Figure Captions

Figure 23. Photograph of hand specimen of gabbro fragment showing coarse-grained, nonlaminated nature. No layering was apparent at the scale of the recovered material (Sample 180-1117A-13R-1, 19–23 cm).

Figure 24. Plots of diabases and metadiabases from Sites 1109, 1114, 1117 and 1118 where they were recovered in situ. Samples from the other holes are normalized to values from Site 1109 (presumed closest to pristine diabase). av. = average.

Figure 25. Plot of diabase and metadiabase samples from talus samples at Sites 1108, 1111, and 1114 normalized to the average values for unaltered diabase from Site 1109. Key: 1 = foliated, epidote-rich schist in Hole 1111A (Sample 180-1111A-16R-CC, 8–15 cm); 2 = metadiabase pebble in sediments of Hole 1108B (Sample 180-1108B-47R-CC, 1–3 cm); 3 = nonfoliated metadiabase in Hole 1114A (Sample 180-1114A-36R-2, 40–42 cm); 4 = foliated metadiabase pebble in Hole 1114A (Sample 180-1114A-36R-1, 70–72 cm).

Figure 26. Plot of major and trace elements of diabases and metadiabases from Sites 1108, 1109, 1111, 1114, 1117, and 1118 normalized to E-MORB using the values of Sun and McDonough (1989).

Figure 27. Close-up photograph of highly sheared gabbro with a well developed foliation plane and shear bands (Sample 180-1117A-9R-1, 24–32 cm).

Figure 28. Core photograph of the fault gouge recovered at Site 1117. This shows soft, light-colored clayey material that contains talc, chlorite, calcite, ankerite, and serpentine. This material is consistent with intense shearing and hydrothermal alteration of underlying deformed gabbro.

Figure 29. Schematic cross section showing the increasing proportion (circles) of strike-slip and oblique-slip faults toward the Moresby Seamount. Note that oblique- and strike-slip faults at Sites 1109 and 1115 occur in the pre-rift sequence.

Figure 30. Estimated thermal gradients (in °C/km) from Leg 180. Confidence in data is discussed in the text.

Figure 31. Plot of dissolved Ca, Mg, and SiO_2 at northern Woodlark Rise sites. The shapes of the Ca and Mg profiles reflect the effects of carbonate diagenesis and a variable extent of alteration of volcanic matter in the upper portion of the sedimentary column of each site. Deeper downhole, alteration of volcanics exerts a more dominant control on pore-water profiles. Large increases in dissolved Ca result primarily from alteration of plagioclase whereas depletion of Mg reflects its uptake during authigenic smectite formation. The dissolved SiO_2 profiles depict a downhole progression including dissolution of volcanic ash in the upper sedimentary column, and WST reactions deeper downhole. Particularly elevated SiO_2 concentrations deep in Site 1118 are attributable to an abundance of fresh to slightly altered volcanic matter in higher porosity sediments.

Figure 32. Biogeochemical profiles in sediments from the Woodlark Basin, Leg 180: **A.** Total bacterial populations at Sites 1109, 1115, and 1118. The solid curve represents a general regression line of bacterial numbers vs. depth in deep-sea sediments (Parkes et al., 1994), with 95% upper and lower prediction limits shown by dashed curves. Sulfate, ammonia, and methane depth profiles at Sites (**B**) 1118, (**C**) 1109, and (**D**) 1115. Unconformity at each site represented by wavy line. **E.** C_1/C_2 ratios at Sites 1108, 1109, 1115, and 1118.

Figure 33. Natural gamma ray from the triple-combo runs in Holes 1114A, 1118A, 1109D, and 1115C.

Figure Captions Continued

Figure 34. Neutron porosity and density porosity from the triple-combo runs in Holes 1114A, 1118A, 1109D, and 1115C.

Figure 35. Photoelectric effect (PEFL) from the triple-combo runs in Holes 1114A, 1118A, 1109D, and 1115C.

Figure 36. Sonic velocity *(V_p)* from the array sonic tool in Holes 1114A, 1118A, 1109D, and 1115C.

Figure 37. This dynamically normalized, double pass FMS image from Site 1115 shows well defined, flat-lying, conductive clayey layers interbedded with thin (~10 cm), resistive sandy or carbonate-rich beds, which are characteristic of the stratigraphy observed in FMS images from each of the three hanging wall drill sites (1109, 1115, and 1118). The dashed lines mark the Pad 1 azimuth trace of each FMS pass. The FMS images are oriented from 0° to 360° from geographic north.

Figure 38. Statically normalized FMS image (left) and tadpole plot (right) from Site 1114. Sinusoidal fit to dipping beds (dashed) and fractures (solid) are used to measure dips and dip directions, which are shown on the tadpole plot. Dominant bed dips are ~30° oriented northwest, while dominant fracture dips are ~50° to ~60° oriented north within the same interval.

Figure 39. Bed and fracture dip direction distributions from Site 1114. **A**, **B.** Histograms of bed and fracture dip directions. **C, D.** Rose diagrams of bed and fracture strikes. The two main populations consist of beds that strike northeast and fractures that strike just north of east.

Figure 40. Depth converted multichannel seismic (MCS) traces at Sites 1118 and 1109, displayed with the lithostratigraphic columns. The MCS data in time, spanning the two sites, is shown correlated with depth. CMP = common midpoint. TWT = two-way traveltime. Lithologic patterns as in Figure 9.

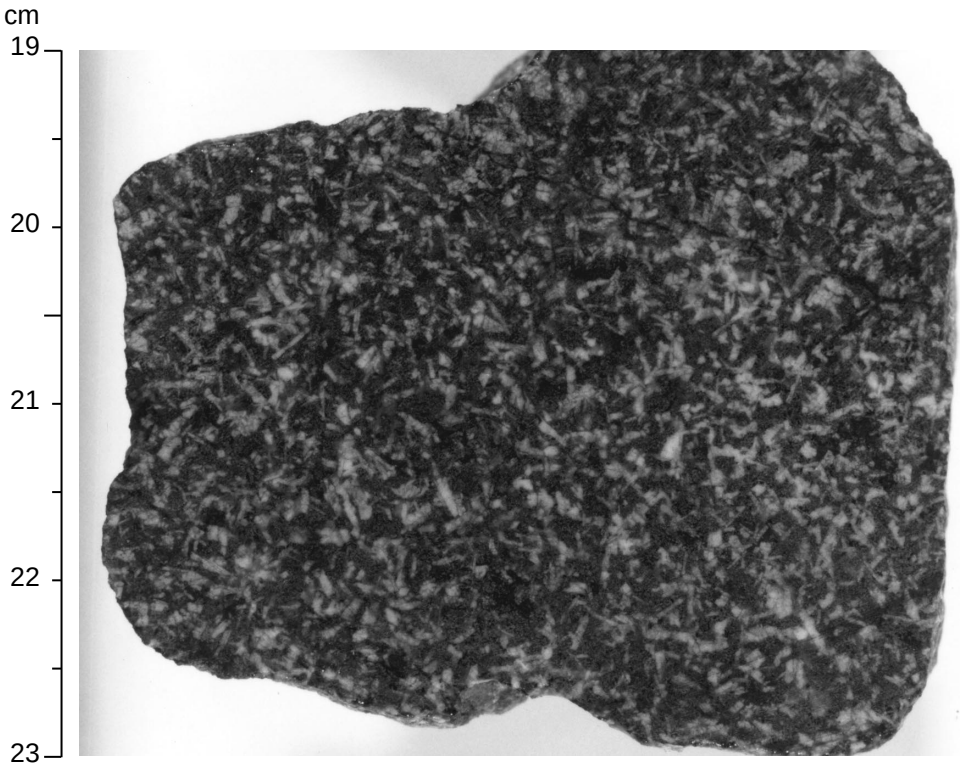

Figure 23

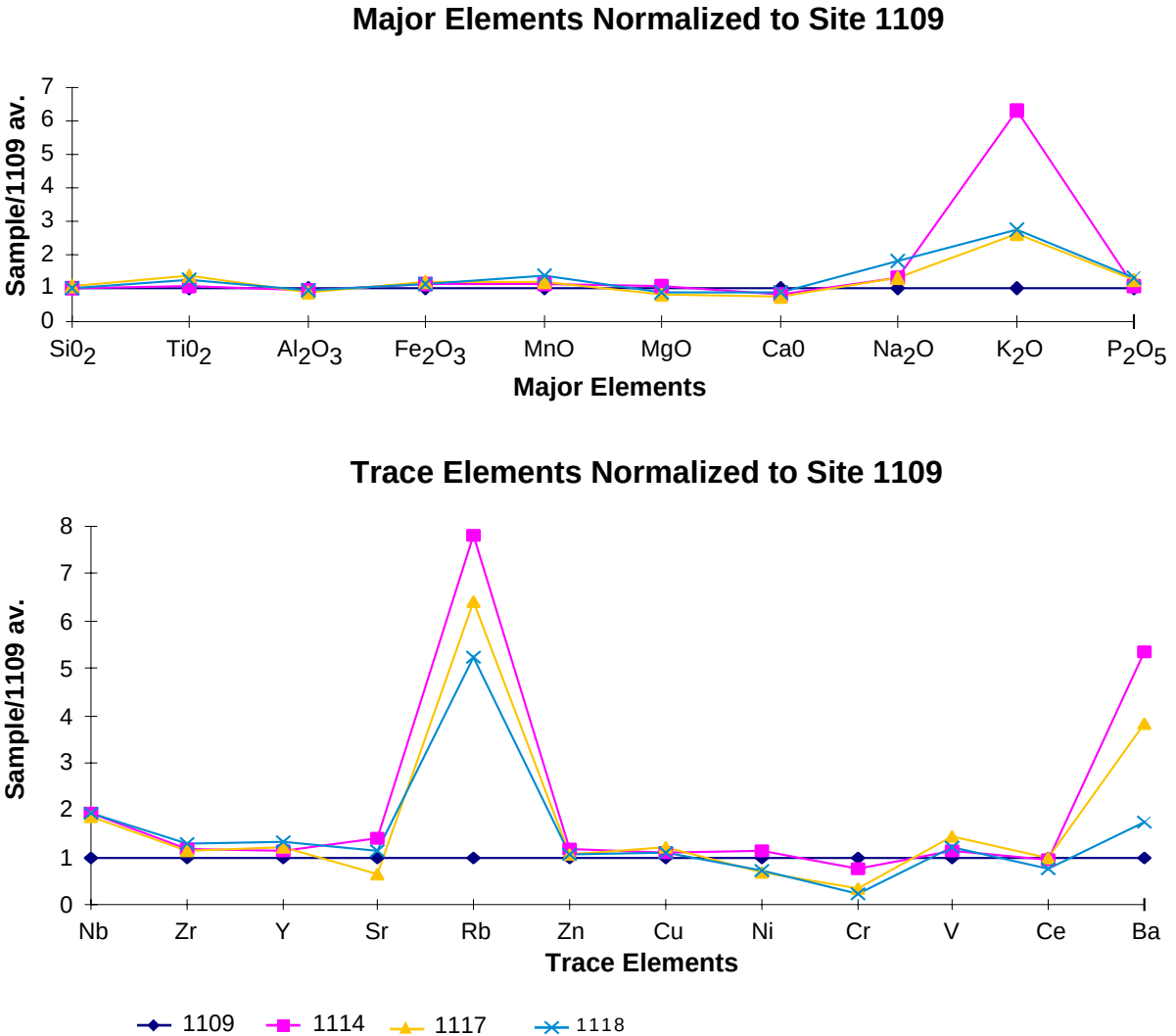
Major Elements Normalized to Site 1109
Sample/1109 av.
0
1
2
3
4
5
6
7
Si0$_2$
Ti0$_2$
Al$_2$O$_3$
Fe$_2$O$_3$
MnO
MgO
Ca0
Na$_2$O
K$_2$O
P$_2$O$_5$
Major Elements
Trace Elements Normalized to Site 1109
Sample/1109 av.
0
1
2
3
4
5
6
7
8
Nb
Zr
Y
Sr
Rb
Zn
Cu
Ni
Cr
V
Ce
Ba
Trace Elements
1109
1114
1117
1118

Figure 24

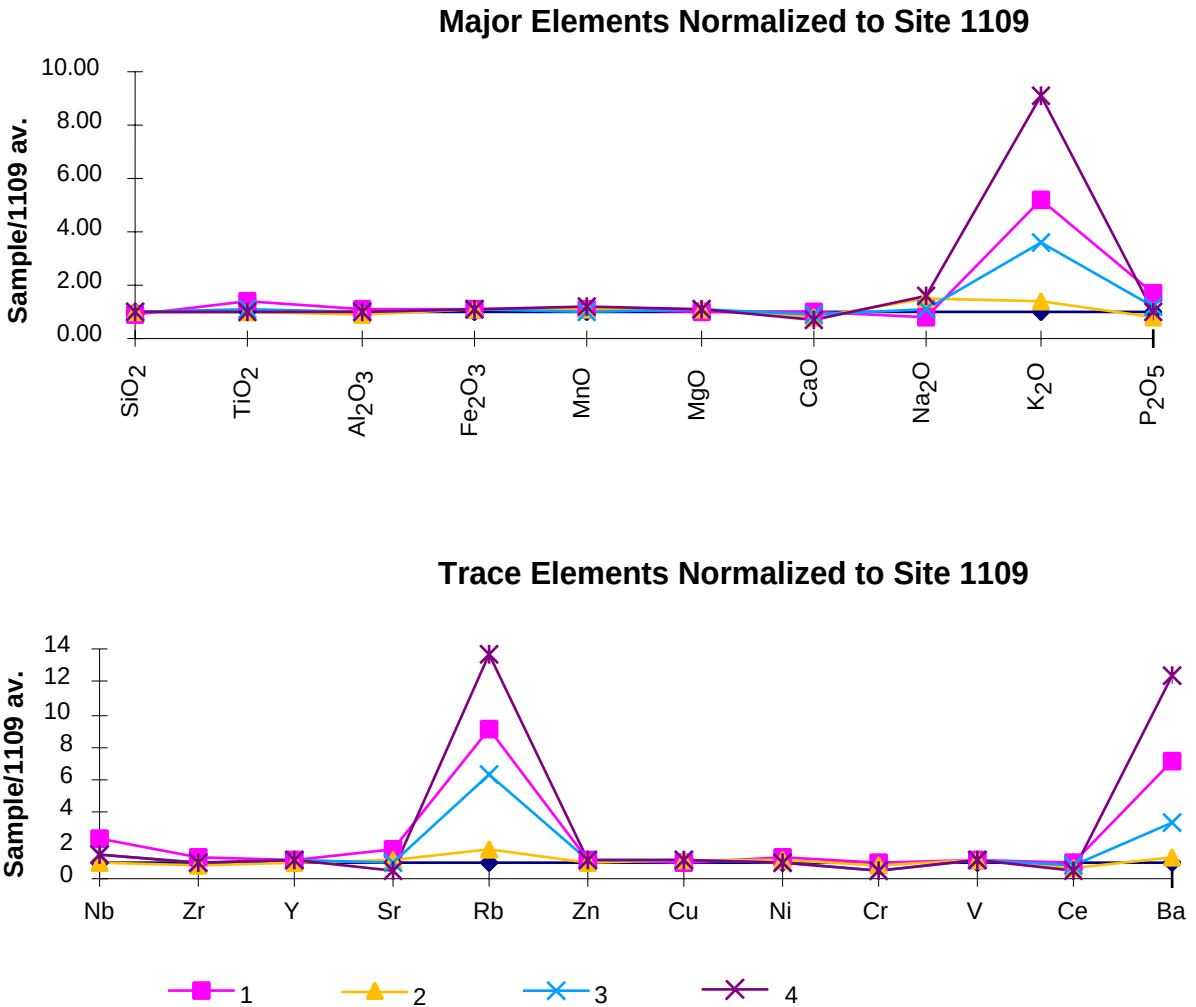
Major Elements Normalized to Site 1109
Sample/1109 av.
10.00
8.00
6.00
4.00
2.00
0.00
SiO2
TiO2
Al2O3
Fe2O3
MnO
MgO
CaO
Na2O
K2O
P2O5
Trace Elements Normalized to Site 1109
Sample/1109 av.
14
12
10
8
6
4
2
0
Nb
Zr
Y
Sr
Rb
Zn
Cu
Ni
Cr
V
Ce
Ba
1
2
3
4

Figure 25

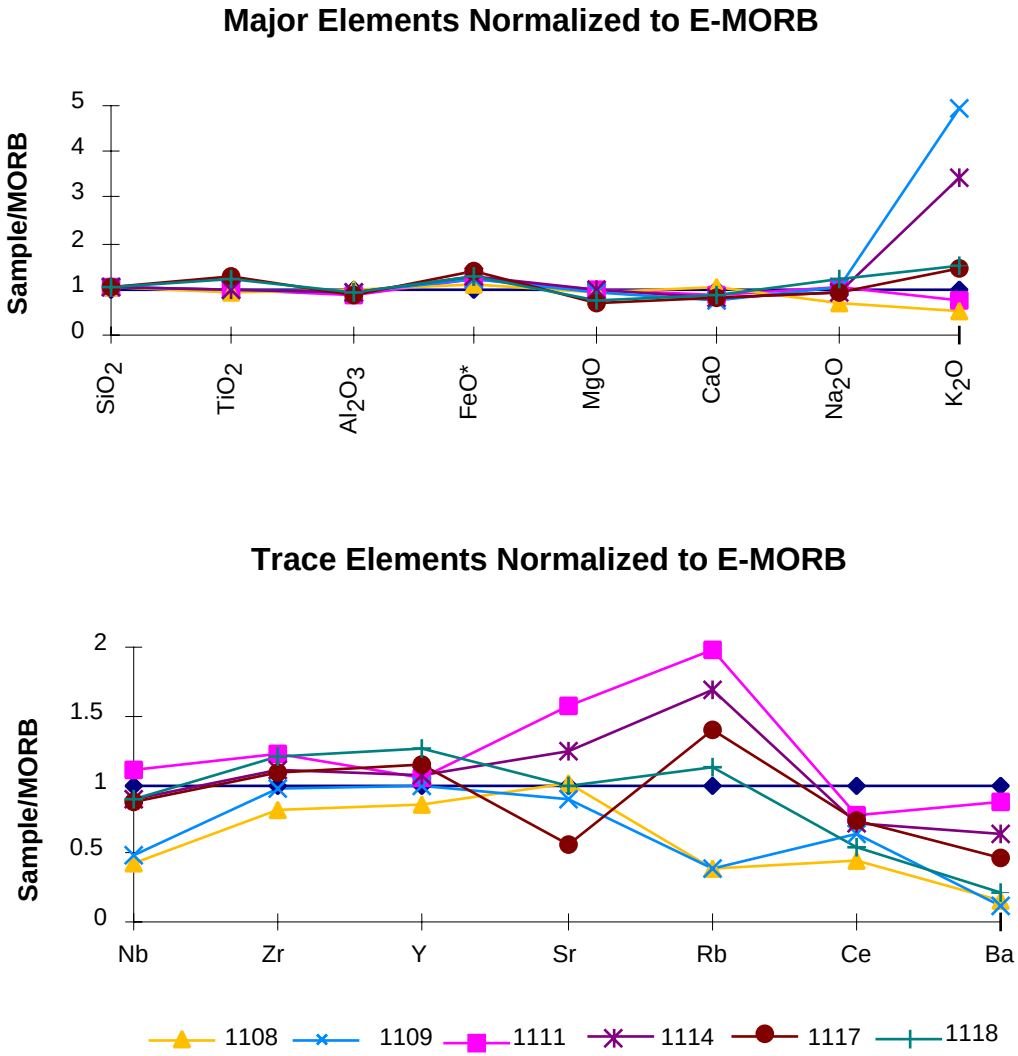
Major Elements Normalized to E-MORB
Sample/MORB
5
4
3
2
1
0
SiO2
TiO2
Al2O3
FeO*
MgO
CaO
Na2O
K2O
Trace Elements Normalized to E-MORB
Sample/MORB
2
1.5
1
0.5
0
Nb
Zr
Y
Sr
Rb
Ce
Ba
1108
1109
1111
1114
1117
1118

Figure 26

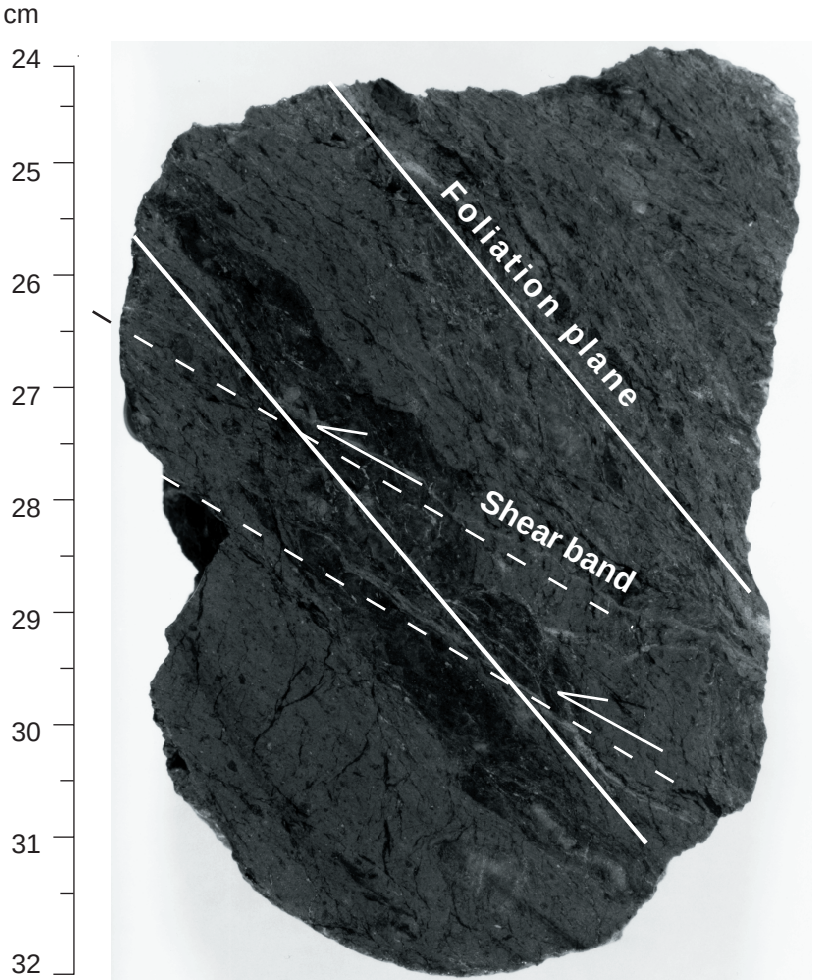

Figure 27

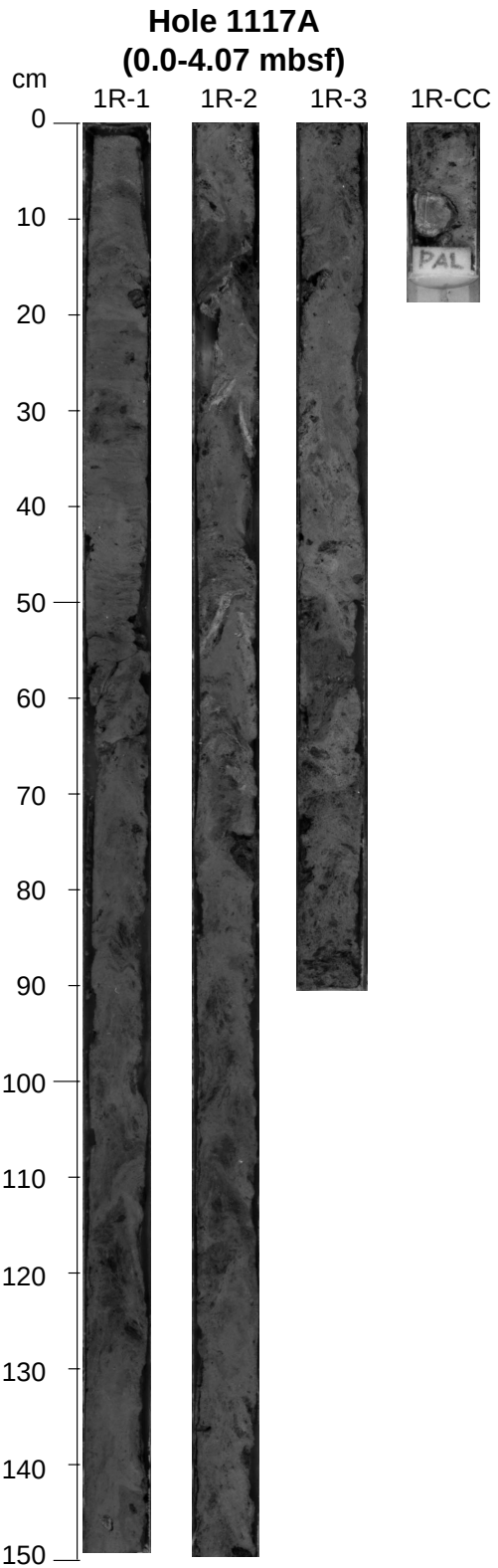
Hole 1117A
(0.0-4.07 mbsf)
cm
1R-1
1R-2
1R-3
1R-CC
0
10
20
30
40
50
60
70
80
90
100
110
120
130
140
150
PAL

Figure 28

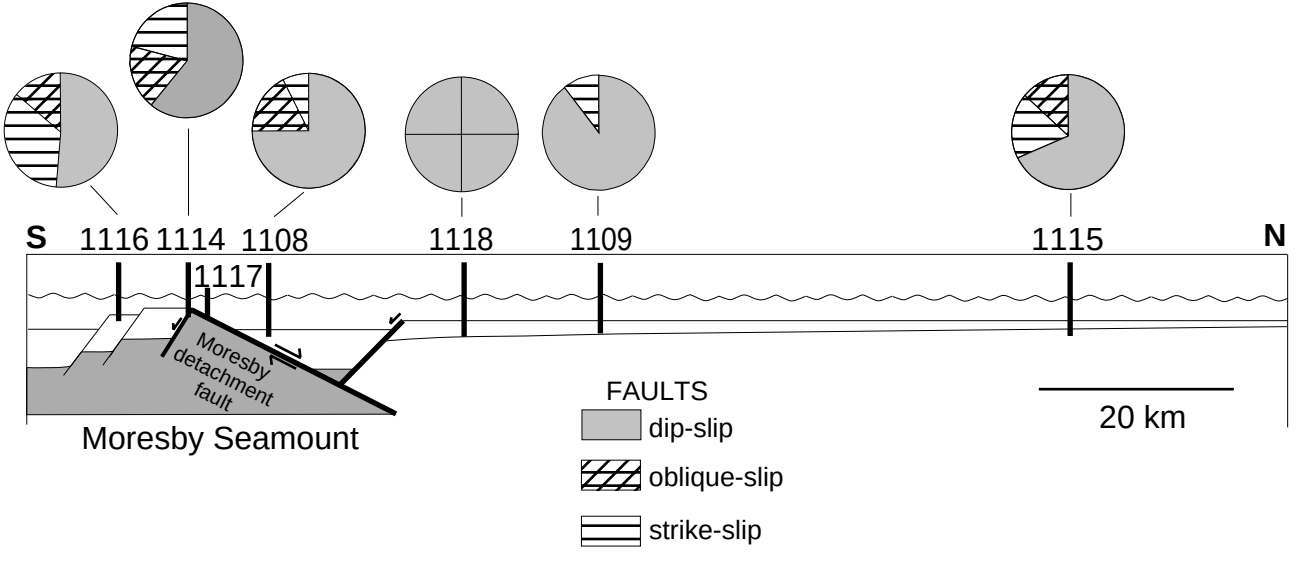
S
1116
1114
1108
1118
1109
1115
N
1117
Moresby detachment fault
Moresby Seamount
FAULTS
dip-slip
oblique-slip
strike-slip
20 km

Figure 29

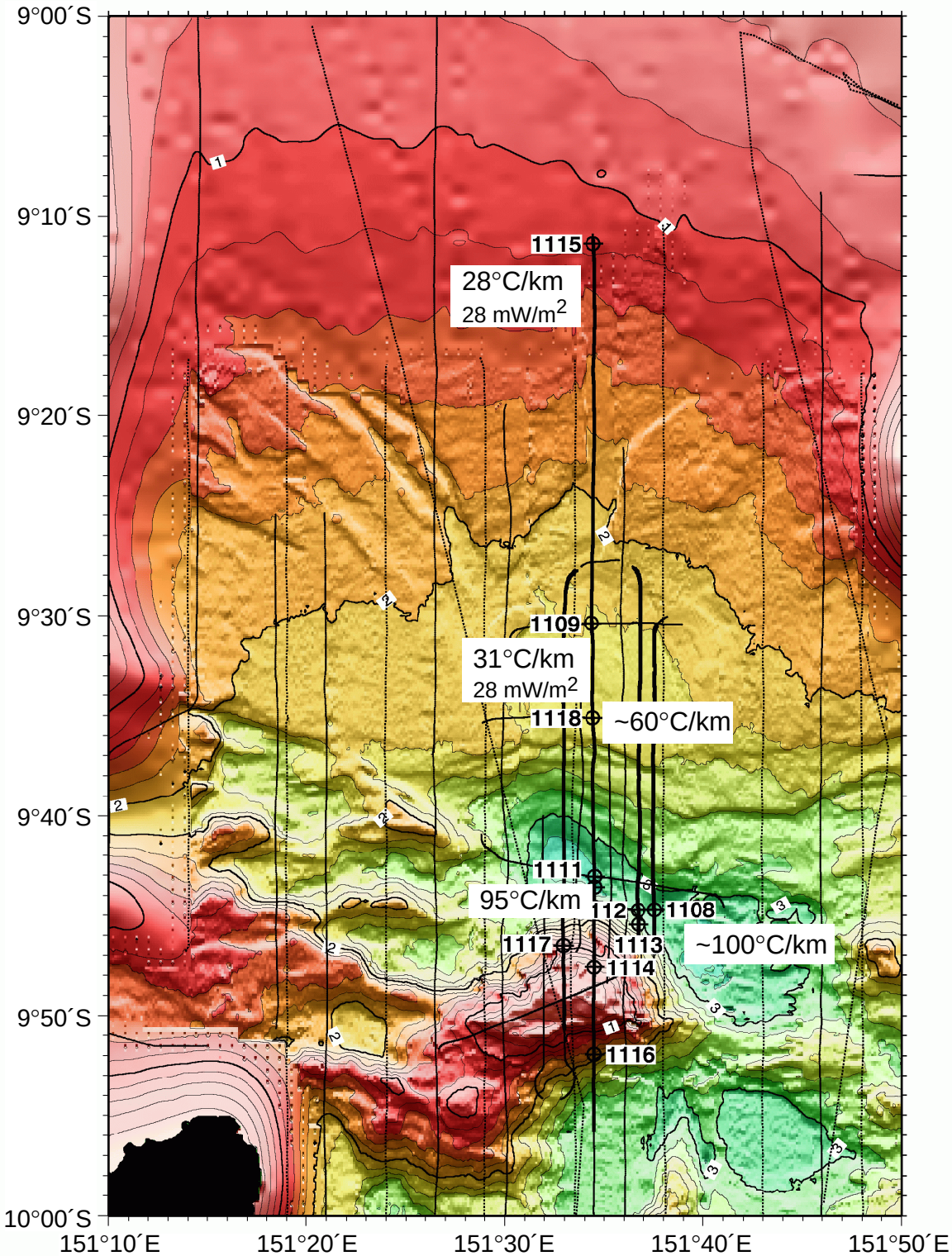
9°00´S
9°10´S
9°20´S
9°30´S
9°40´S
9°50´S
10°00´S
151°10´E
151°20´E
151°30´E
151°40´E
151°50´E
1115
28°C/km
28 mW/m2
1109
31°C/km
28 mW/m2
1118
~60°C/km
1111
95°C/km
112
1108
1117
1113
1114
~100°C/km
1116

Figure 30

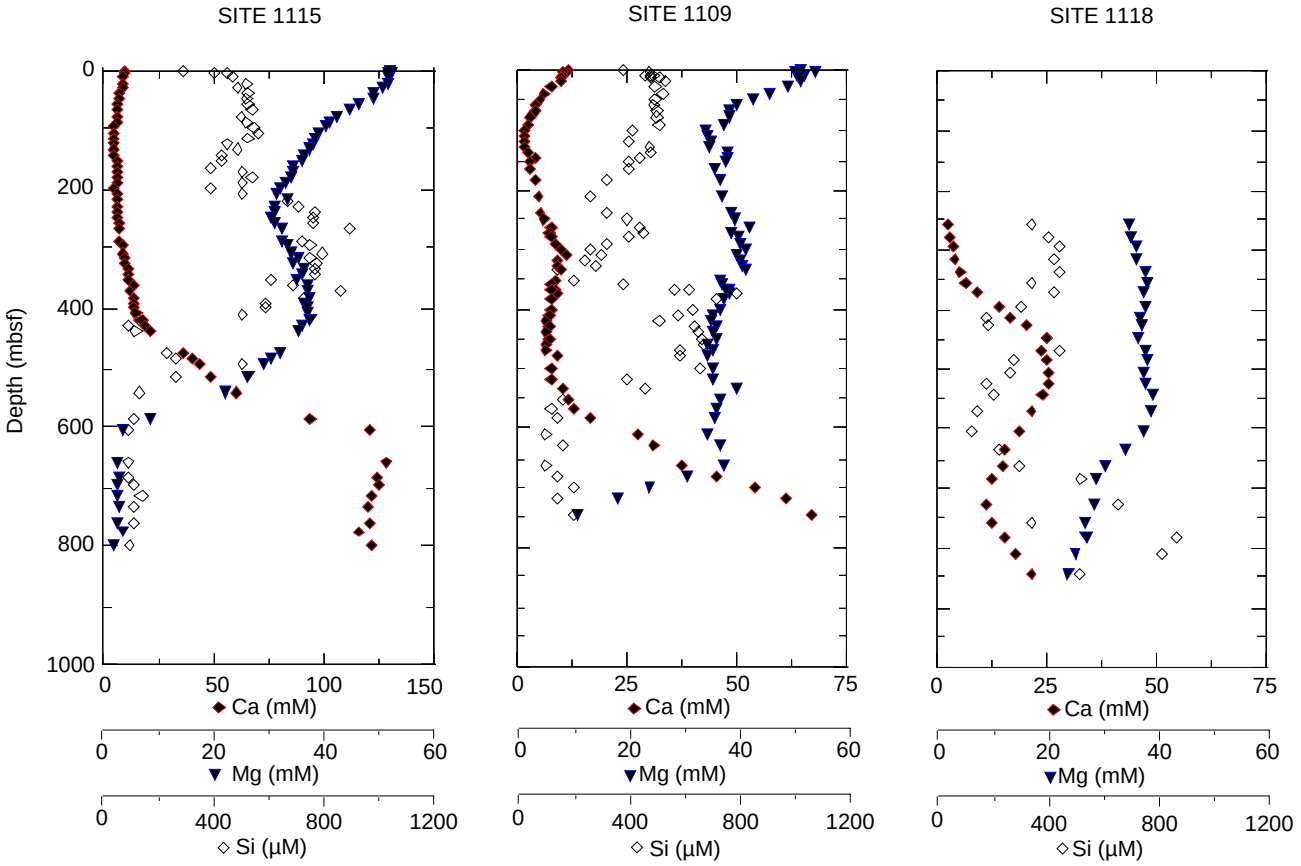
SITE 1115
SITE 1109
SITE 1118
Depth (mbsf)
0
200
400
600
800
1000
0
50
100
150
Ca (mM)
0
20
40
60
Mg (mM)
0
400
800
1200
Si (µM)
0
25
50
75
Ca (mM)
0
20
40
60
Mg (mM)
0
400
800
1200
Si (µM)
0
25
50
75
Ca (mM)
0
20
40
60
Mg (mM)
0
400
800
1200
Si (µM)

Figure 31

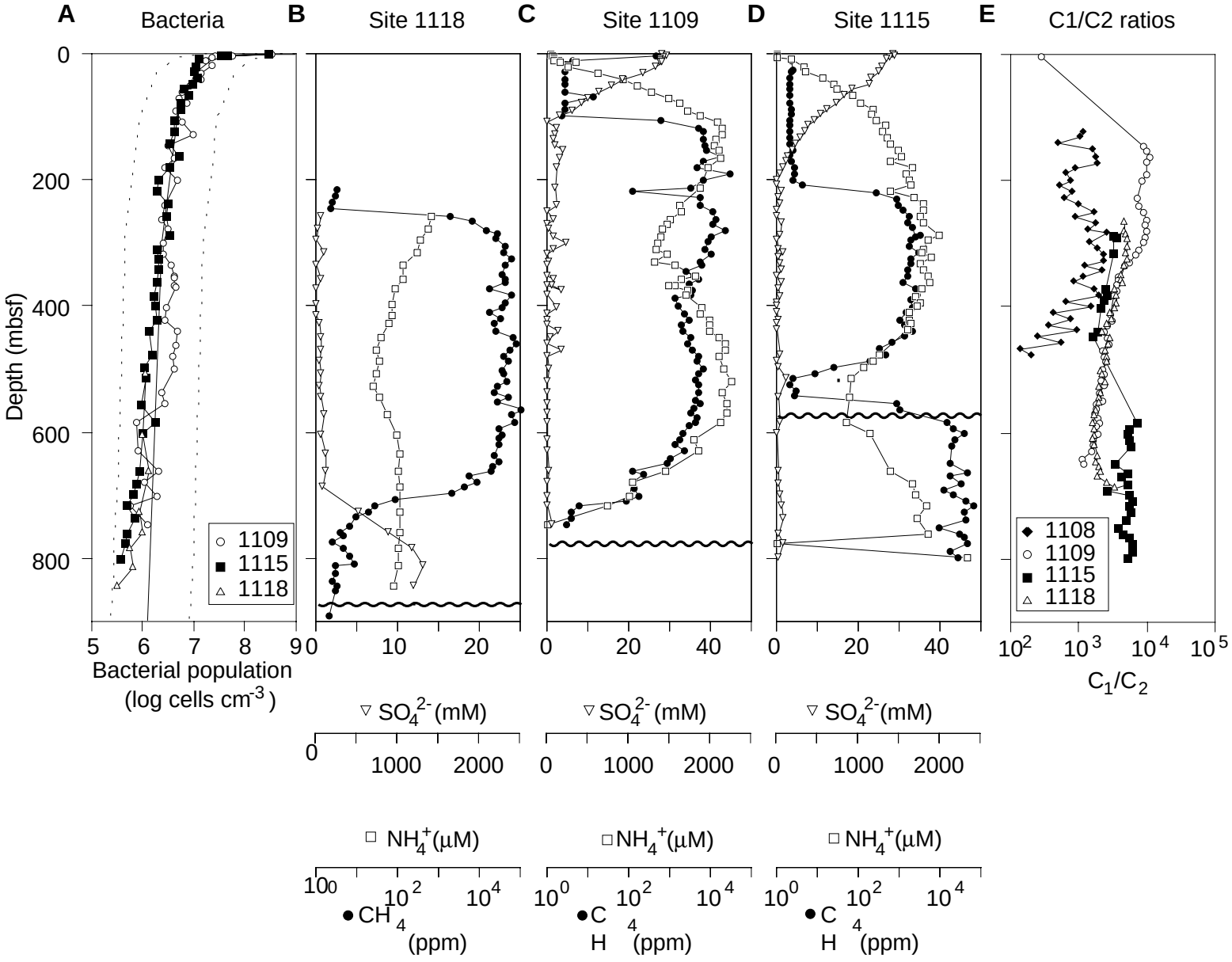
A
Bacteria
B
Site 1118
C
Site 1109
D
Site 1115
E
C1/C2 ratios
Depth (mbsf)
0
200
400
600
800
1109
1115
1118
5
6
7
8
9
Bacterial population
(log cells cm-3)
0
10
20
0
20
40
0
20
40
1108
1109
1115
1118
10^2
10^3
10^4
10^5
C1/C2
SO4 2- (mM)
0
1000
2000
NH4+(µM)
10^0
10^2
10^4
CH4 (ppm)

Figure 32

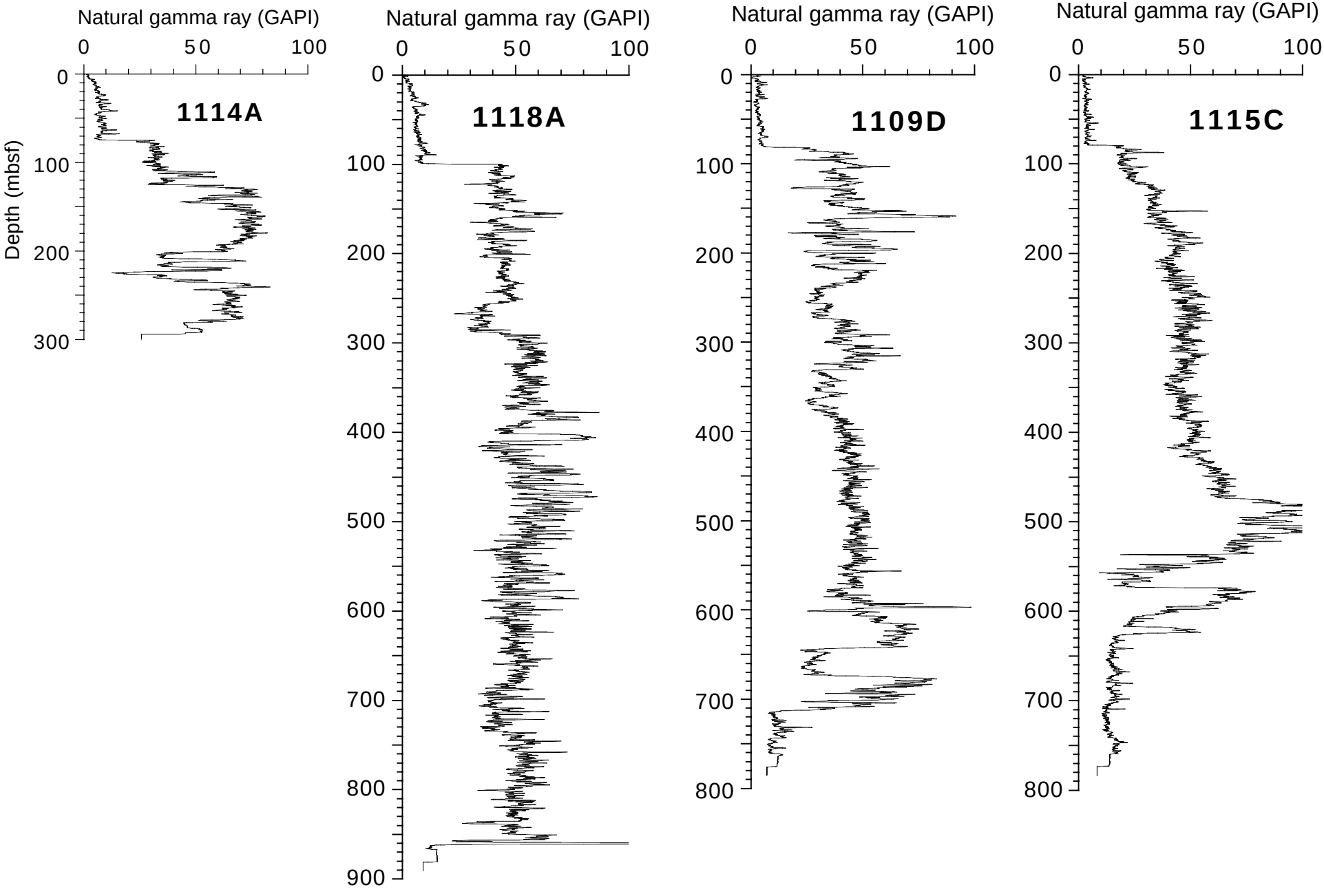
Natural gamma ray (GAPI)
0
50
100
Depth (mbsf)
1114A
1118A
1109D
1115C

Figure 33

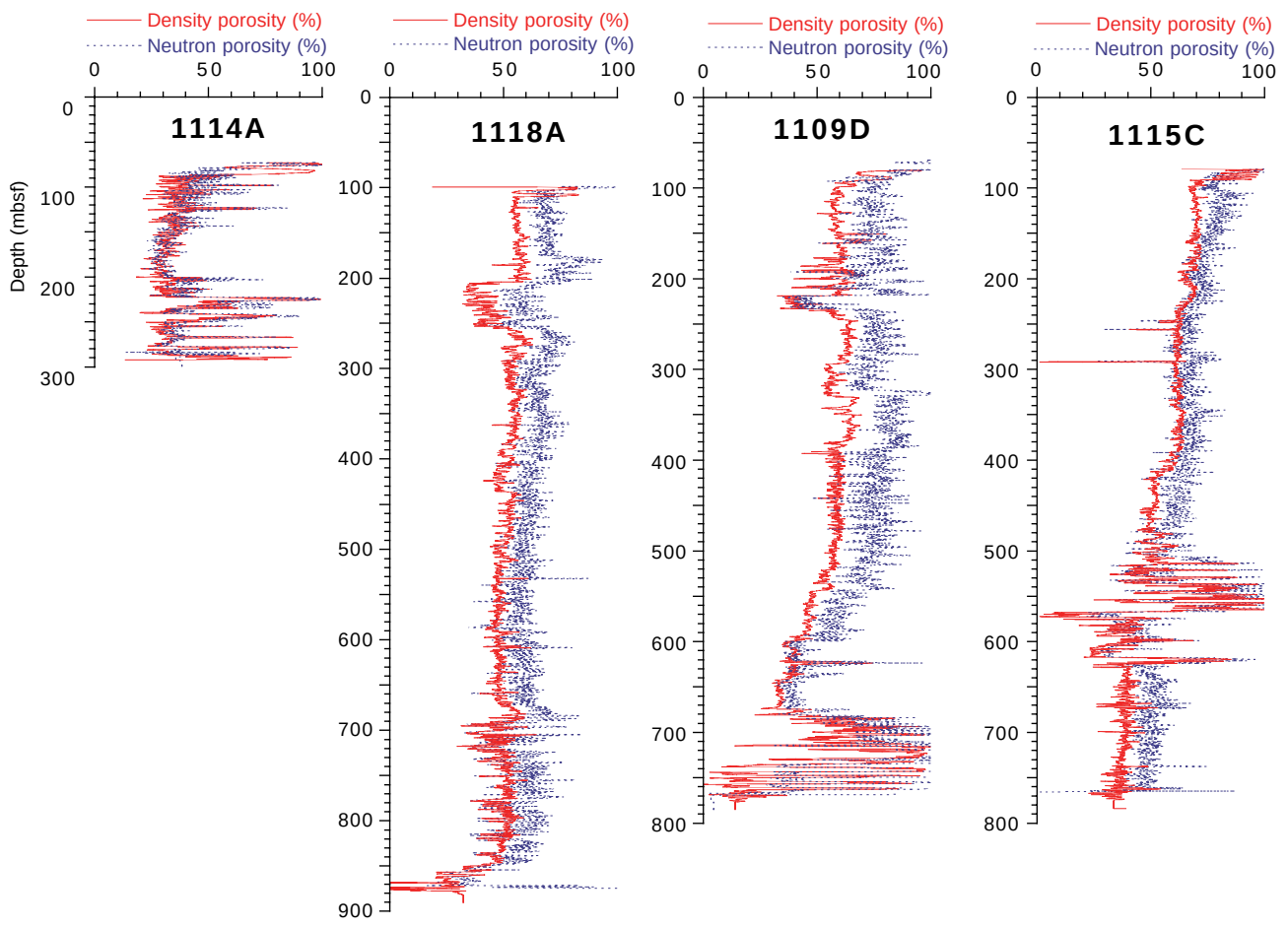
Density porosity (%)
Neutron porosity (%)
0
50
100
1114A
1118A
1109D
1115C
Depth (mbsf)
0
100
200
300
400
500
600
700
800
900

Figure 34

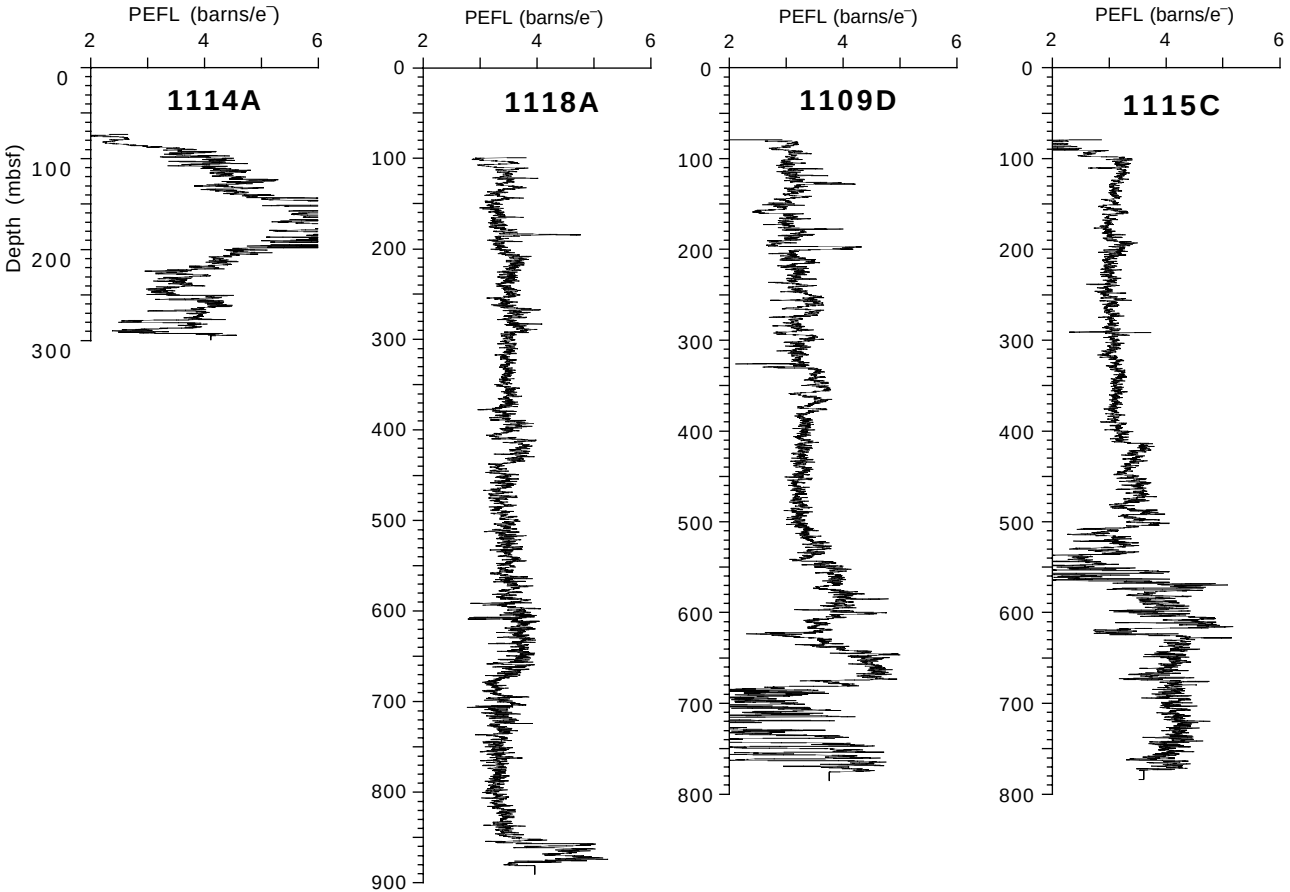
PEFL (barns/e⁻)
2
4
6
Depth (mbsf)
0
100
200
300
1114A
1118A
400
500
600
700
800
900
1109D
1115C

Figure 35

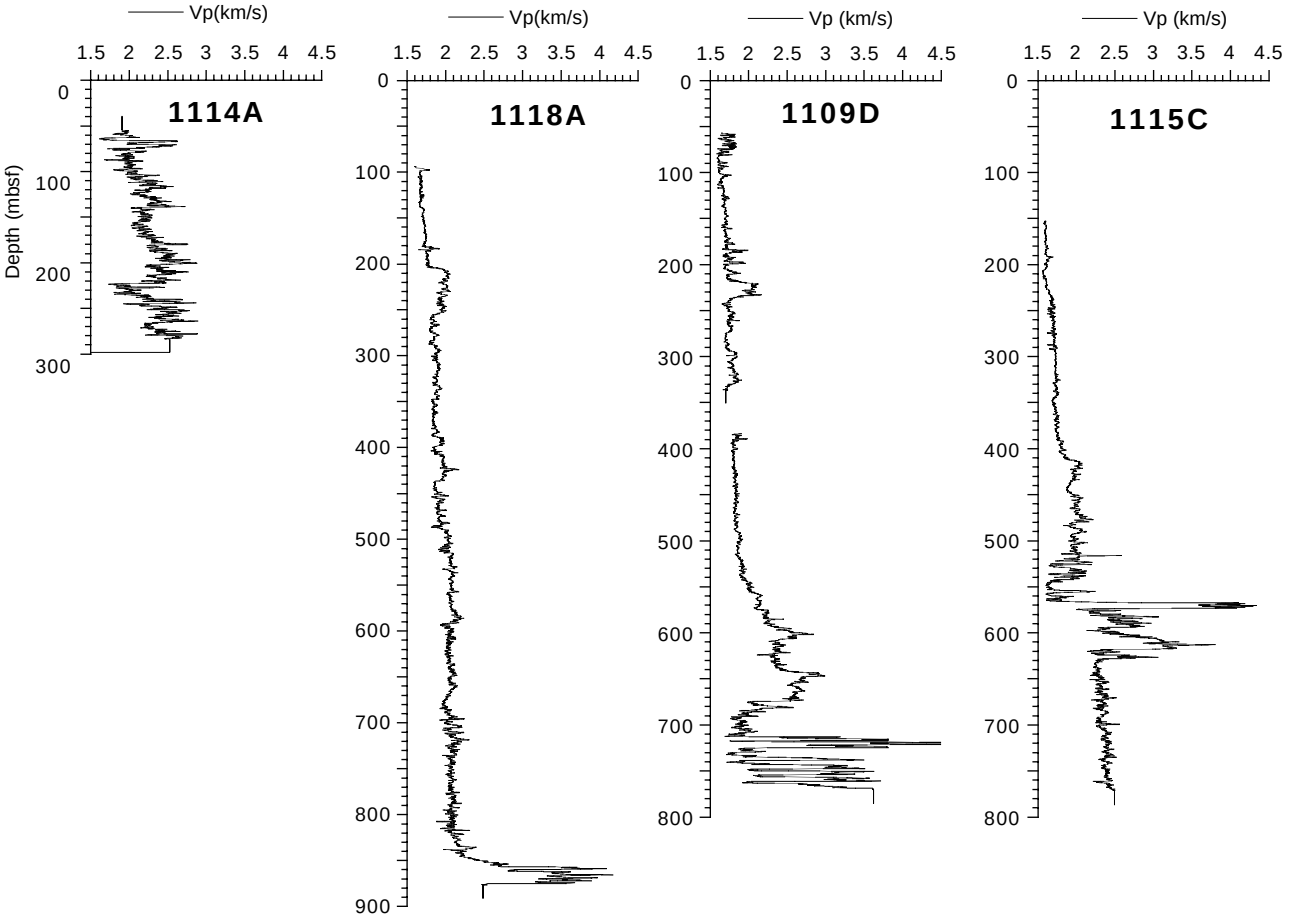
Vp(km/s)
1.5 2 2.5 3 3.5 4 4.5
1114A
Depth (mbsf)
0 100 200 300
Vp(km/s)
1.5 2 2.5 3 3.5 4 4.5
1118A
0 100 200 300 400 500 600 700 800 900
Vp (km/s)
1.5 2 2.5 3 3.5 4 4.5
1109D
0 100 200 300 400 500 600 700 800
Vp (km/s)
1.5 2 2.5 3 3.5 4 4.5
1115C
0 100 200 300 400 500 600 700 800

Figure 36

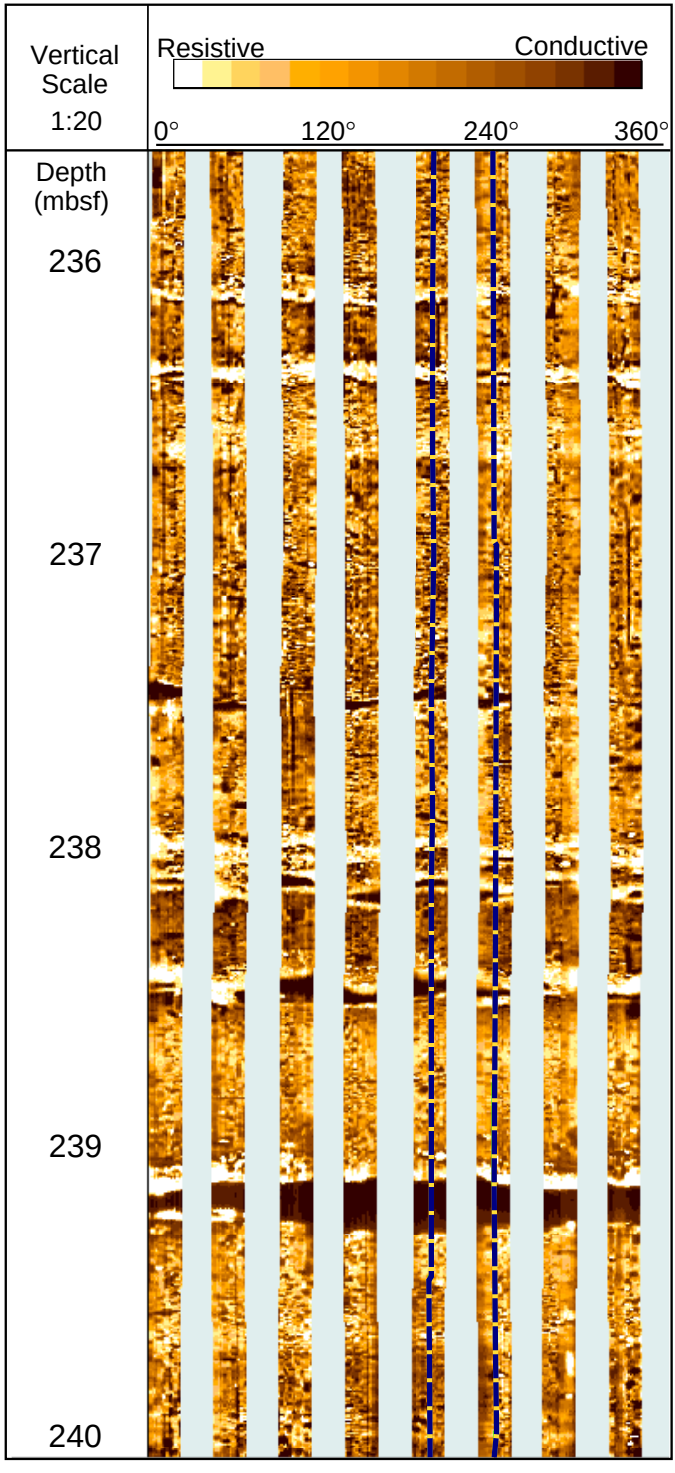
Vertical Scale 1:20
Resistive
Conductive
0°
120°
240°
360°
Depth (mbsf)
236
237
238
239
240

Figure 37

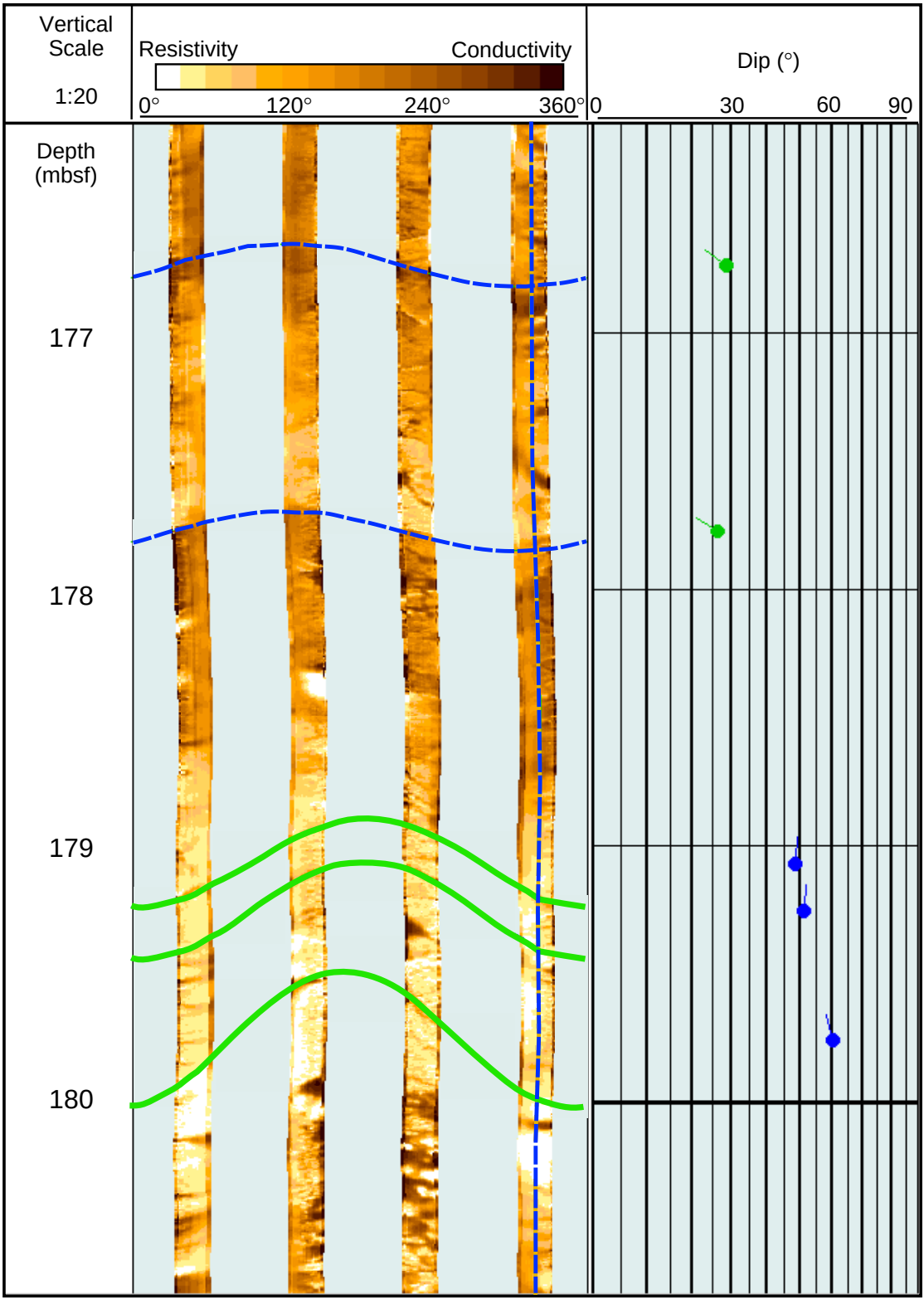
Vertical Scale
1:20
Resistivity
Conductivity
0°
120°
240°
360°
Dip (°)
0
30
60
90
Depth (mbsf)
177
178
179
180

Figure 38

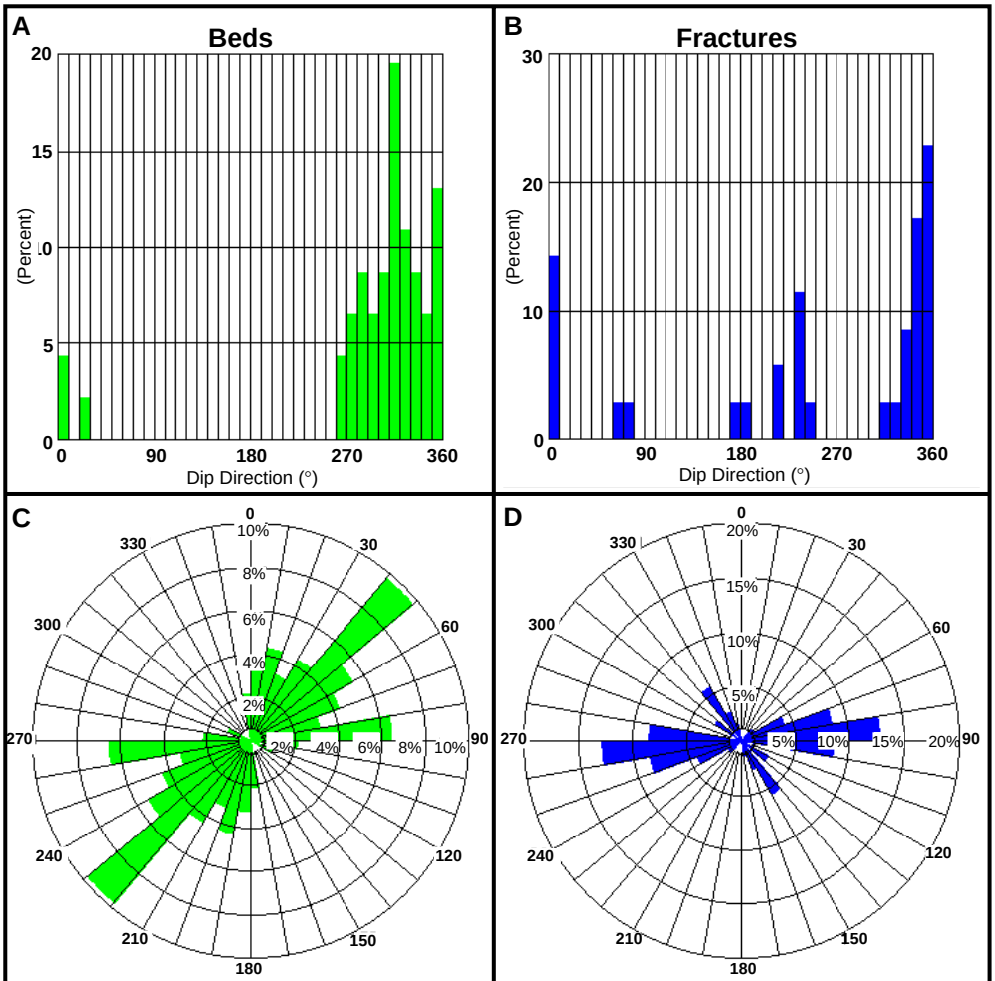
A
Beds
(Percent)
Dip Direction (°)
B
Fractures
(Percent)
Dip Direction (°)
C
D

Figure 39

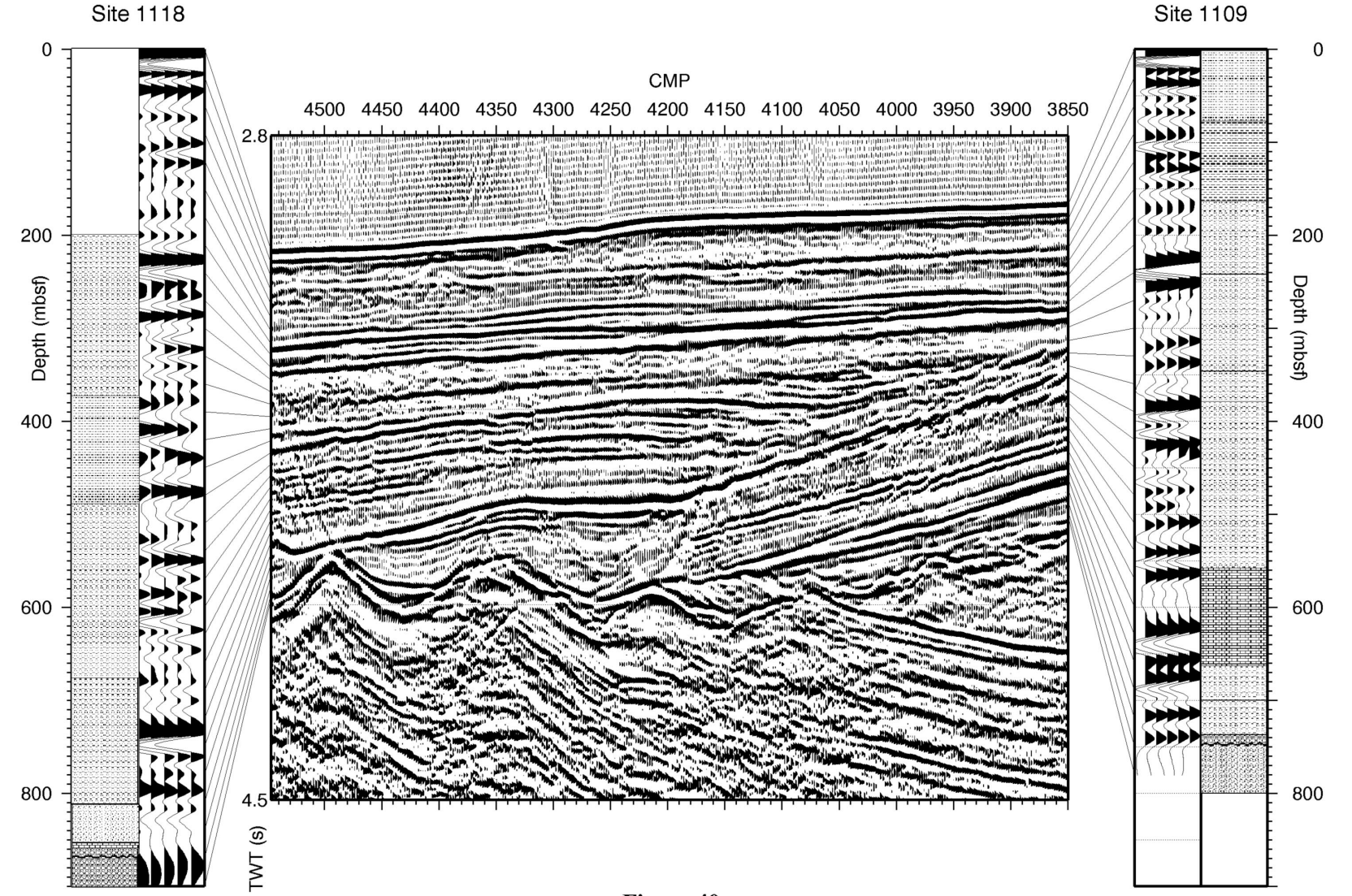
Site 1118
Site 1109
CMP
4500 4450 4400 4350 4300 4250 4200 4150 4100 4050 4000 3950 3900 3850
2.8
4.5
TWT (s)
Depth (mbsf)
0
200
400
600
800

Figure 40